Solar Light Activated Periodate for Degradation and Detoxification of 2 Highly Toxic 6PPD-Quinone at Environmental Levels

Solar Light Activated Periodate for Degradation and Detoxification of Highly Toxic 6PPD-Quinone at Environmental Levels

Long Chen [1, 2], Jingrun Hu [1], Alistair G.L. Borthwick [3, 4], Weiliang Sun [5], Huixuan Zhang [1], Dantong Jia [1], Wen Liu [1, 2, *]

[1] *College of Environmental Sciences and Engineering, The Key Laboratory of Water and Sediment Sciences (Ministry of Education), Peking University, Beijing 100871, PR China*

[2] *International Joint Laboratory for Regional Pollution Control (Ministry of Education), Peking University, Beijing, 100871, PR China*

[3] *Institute of Infrastructure and Environment, School of Engineering, The University of Edinburgh, King's Buildings, Edinburgh EH9 3JL, UK*

[4] *School of Engineering, Computing and Mathematics, University of Plymouth, Drake Circus, Plymouth PL4 8AA, UK*

[5] *Department of Civil and Environmental Engineering, Louisiana State University, Baton Rouge 70803, LA, USA*

***Corresponding author**

Tel: +86-15810726268; E-mail: wen.liu@pku.edu.cn

Abstract

Degradation and detoxication of highly toxic 6PPD-quinone remain great challenges due to its stable structure. Herein, we establish a solar-light-driven IO_4^- activation system for efficient degradation of 6PPD-quinone at environmental concentration levels (10–100 μg L^{-1}), with residual concentration below 5.7 ng L^{-1} (detection limit) within 30 min. $IO_3^•$ was determined as the primary reactive species after IO_4^- activation for cleavage of the highly toxic quinone structure. Single electron transfer (SET) is the most favorable route for $IO_3^•$ attacking, in which single electrons achieve self-driven transfer from 6PPD-quinone to $IO_3^•$ due to the maintenance of spatial inversion symmetry generated by dipole moments. Femtosecond transient absorption spectra (fs-TAS) confirmed the formation of 6PPD-quinone cationic radical (6PPD-quinone$^{•+}$), which was the key reaction intermediate. This study proposes a promising technology for degradation and detoxification of high-toxic 6PPD-quinone in water, and brings deep insight into the reaction mechanism within IO_4^- activation systems.

Introduction

Tire-wear particles (TWP) are an important source of rainwater runoff pollution, which can release toxic pollutants with teratogenic, mutagenic, and estrogen effects[1, 2]. Among them, 6PPD (N-(1,3-dimethylbutyl)-N′-phenyl-p-phenylenediamine) is a widely used antioxidant and antiozonant in rubber tires[3, 4]. In the aerobic environment, 6PPD can transform into 6PPD-quinone (N-(1,3-dimethylbutyl)-N′-phenyl-p-phenylenediamine-quinone), which is a matter of great concern due to the high toxicity of 6PPD-quinone to aquatic organisms[5, 6]. 6PPD-quinone is a newly discovered emerging micropollutant, and so its detection and removal are very cutting-edge research topics.

In the water matrix, 6PPD-quinone is formed through oxidation of 6PPD by singlet oxygen ($^1O_2$) in the ozone environment, through a series transformation process including amine group oxidation, side-chain oxidation and nitroxide radical formation (**Fig. 1a**)[7, 8, 9]. Thus, the high toxicity of 6PPD-quinone is attributed to the formed quinone structure[10, 11, 12]. In addition, 6PPD-quinone is more stable in water than 6PPD because the hydrolysis half-life of 6PPD-quinone (12.8–16.3 d) is much longer than that of 6PPD (0.2–2.7 h)[13], leading to persistent toxic effects on sensitive organisms[10, 14]. 6PPD-quinone has been widely detected in road runoff, tire rubber leachate and road dust, especially in natural waters[6, 10, 15]. The high toxicity of 6PPD-quinone poses a great threat to drinking water safety, and so effective treatment technologies are urgently required. However, to the best of our knowledge, the degradation and removal of 6PPD-quinone in water have not been investigated to date.

Advanced oxidation processes (AOPs) can achieve rapid degradation and even mineralization of organic pollutants due to the production of reactive radicals[16, 17]. Recently, periodate-based AOP has attracted increasing interest regarding the degradation of micro-pollutants because of its advantageous generation of iodine-related radicals with high electrophilicity besides the conventional hydroxyl radical ($^{\bullet}OH$)[18, 19]. $IO_3^{\bullet}$ is considered the

most important species in periodate-based AOPs[20, 21]. Specifically, $IO_3^{\bullet}$ achieves stronger electronic delocalization, where the free electron is delocalized on three oxygen atoms through resonance effect, thus occupying the low-energy single occupied molecular orbital (SOMO) for effective electrophilic attack[22]. However, research is very limited concerning the reaction mechanism of $IO_3^{\bullet}$-induced oxidation of organic compounds, especially the reaction route dependency of radical adduct formation (RAF), hydrogen atom abstraction (HAA), and single electron transfer (SET)[23, 24]. Moreover, the difference in reaction mechanism of electron distribution and transfer behavior at the molecular orbital level for $IO_3^{\bullet}$/$^{\bullet}OH$ is also unclear.

In this study, we report an AOP system of IO_4^- activation under solar light irradiation (solar/IO_4^-) to degrade 6PPD-quinone at environmental levels. The detoxification performance of 6PPD-quinone was evaluated by degradation kinetics, degradation pathway and toxicity to zebrafish embryos (**Figs. 1b-1c**). Dynamic electron distribution analysis was performed to deeply reveal the reaction mechanism. Additionally, the efficiency of solar/IO_4^- technology for the removal of 6PPD-quinone in real water bodies under natural solar light was also evaluated for practical application. This study not only advances the understanding of $IO_3^{\bullet}$-initiated reaction mechanisms for organics degradation, but also proposes an efficient technology for the removal of 6PPD-quinone at environmental concentration levels.

Results

Degradation of 6PPD-quinone in solar/IO_4^- system

6PPD-quinone was successfully detected by an ultra-high performance liquid chromatography-mass/mass (UPLC-MS/MS) system, with a retention time (RT) of 9.95 min and a primary mass peak of *m/z* = 299.17477 (**Supplementary Fig. 1**)[10]. The limit of detection (LOD = 5.7 ng L^{-1}) and limit of quantification (LOQ = 19.0 ng L^{-1}) were determined as the lowest concentrations, giving signal to noise (S:N) ratios of 3 and 10, respectively[25]. 6PPD-

quinone did not undergo photolysis or direct oxidation by IO_4^- (< 3%) (**Fig. 2a**). For all three initial concentrations (*i.e.*, 100, 50, and 10 μg L^{-1}), 6PPD-quinone was effectively degraded by activated IO_4^- (0.2 mmol L^{-1}) under simulated solar light. Specifically, 100 μg L^{-1} of 6PPD-quinone was degraded to a final residual concentration of 16.7 ng L^{-1} at 60 min, indicating a ~4 orders of magnitude reduction after degradation (removal efficiency of 99.99%).

The degradation of 6PPD-quinone can be well described by the *pseudo*-first order kinetic model[26], with a rate constant (k_1) of 0.14 min^{-1} (R^2 = 0.98). In comparison, traditional AOPs (solar/H_2O_2 and solar/PDS) at the same condition for 6PPD-quinone degradation showed lower removal efficiencies of 69.2% and 84.1% at 60 min, respectively (**Fig. 2b**). The reaction rate constant in the solar/IO_4^- system was 7.0 and 4.7 times higher than that in the solar/H_2O_2 (k_1 = 0.02 min^{-1}) and solar/PDS (k_1 = 0.03 min^{-1}), respectively (**Supplementary Table 1**). In light-induced homogenous AOPs, the pollutant degradation performance is highly related to the type and concentration of radicals, while the radical concentration is mainly determined by the light absorption coefficient and quantum yield of oxidant[27]. Specifically, under a typical light irradiation of 254 nm, the molar absorption coefficient of IO_4^- (1460 L mol^{-1} cm^{-1}) was much higher than that of H_2O_2 (17.5 L mol^{-1} cm^{-1}) and PDS (25.0 L mol^{-1} cm^{-1}) (**Supplementary Fig. 2**). Moreover, the calculated quantum yield of IO_4^- (1.56 mol $Einstein^{-1}$) was much higher than that of H_2O_2 (0.5 mol $Einstein^{-1}$) and PDS (1.4 mol $Einstein^{-1}$) at 254 nm[28, 29] (**Supplementary Fig. 3** and **Fig. 4**). Given that 6PPD-quinone has typical concentrations of 2–19 μg L^{-1} in runoff and natural water bodies[10, 30], we also investigated the degradation of 6PPD-quinone at a representative environmental concentration of 10 μg L^{-1} (**Fig. 2a**). Interestingly, 6PPD-quinone was completely degraded, with the residual concentration falling below LOD within 30 min. To the authors' knowledge, this is the first time that trace 6PPD-quinone has been degraded.

Zebrafish embryo exposure test was conducted to evaluate the toxicity attenuation during 6PPD-quinone degradation (**Fig. 2c**)[31]. Although the mortality rate (48 h) of zebrafish embryos

115 placed in the initial solution (containing 6PPD-quinone and $NaIO_4$ before reaction) in darkness
116 was 77.8%, the rate in the transformation products (TPs) samples after degradation
117 progressively decreased continuously with reaction time, finally to 10.0% at 120 min.
118 Moreover, for the abnormal development test, when 6PPD-quinone solution samples were
119 taken in the initial reaction period (0–20 min), not all the embryos hatched, but instead
120 presented with pericardial edema[32]. 6PPD-quinone exposure would also induce malformations
121 and cause morphological changes in zebrafish larvae[33]. However, most of the zebrafish
122 embryos hatched normally when placed in the solution sample after 120-min reaction.
123 Therefore, it is demonstrated that the proposed solar/IO_4^- system effectively transformed
124 6PPD-quinone into less toxic TPs. In our tests, the final residual concentration of 6PPD-
125 quinone was invariably lower than the toxicity threshold (95 ng L^{-1}), with some values even
126 lower than the detection limit (**Supplementary Table 2**). This indicates that solar/IO_4^- AOP
127 technology has great practical application potential to treat trace-level 6PPD-quinone in water.
128
129 **ROS production and contribution to 6PPD-quinone degradation**
130 Various reactive oxygen species (ROS) including $IO_3^{\bullet}$, $^{\bullet}OH$, and $^{\bullet}O_2^-$ have been reported
131 to form after IO_4^- activation by light irradiation (**Equations 1–3**)[34]. Scavenger quenching tests
132 evaluated the contribution of produced ROS to 6PPD-quinone degradation (**Fig. 3a**). Addition
133 of *tert*-butyl alcohol (TBA, as a scavenger of $^{\bullet}OH$) only slightly decreased the 6PPD-quinone
134 degradation efficiency at 60 min from 99.9% to 94.5%, with an inhibitory efficiency (η) of
135 5.5%, indicating a very limited contribution of $^{\bullet}OH$, in good accordance with the previous
136 study[35]. A similar minor contribution of $^{\bullet}O_2^-$ was also observed with a slight inhibition effect
137 (η = 3.9%) by Tiron (TI). Excess phenol was generally considered as a scavenger of both $IO_3^{\bullet}$
138 and $^{\bullet}OH$[18], and an obvious inhibition effect (η = 77.6%) on 6PPD-quinone degradation was
139 observed. In addition, atomic oxygen, *i.e.* $O(^3P)$, and O_3 can be also generated in light-induced

IO_4^- AOPs[29]. Isopropanol (IPA) was used as the scavenger both for $^{\bullet}OH$ and $O(^3P)$, and cinnamic acid was used for O_3. The addition of IPA showed a similar inhibition effect to TBA (**Supplementary Fig. 5**), so the role of $O(^3P)$ in the removal of 6PPD-quinone was also limited (η = 6.2%). Addition of cinnamic acid also indicated the low contribution of O_3 (η = 1.89%). Notably, previous studies have reported that the transformation of 6PPD-quinone from 6PPD occurs at the O_3 environment[6, 7, 15], indicating 6PPD-quinone is chemically stable under the attack of O_3.

Reactive iodine species (RIS) (*e.g.*, HOI, I_2, I_3^- and I^-) were not detected in the solar/IO_4^- system (**Supplementary Fig. 6**), while a highly related linear relationship (R^2 = 0.9995) between k_1 and IO_4^- dosage was found (**Supplementary Fig. 7**). This further confirms that $IO_3^{\bullet}$ generated from IO_4^- activation played the primary role in degradation of 6PPD-quinone, with minor contributions from $^{\bullet}OH$ and other reactive species. The quantitative analysis further revealed that 30.3% of IO_4^- (dosage of 0.2 mmol L^{-1}) was converted to non-toxic IO_3^- after 60 min's reaction (**Fig. 3b**). The iodine mass balance also indicated that all IO_4^- was converted into IO_3^- (total IO_4^- and IO_3^- content maintained at 100%). This blocked the possibility of generation of iodinated disinfection byproducts (I-DBPs) since RISs such as HOI, I_2 and I_3^- have a higher activity to oxidize natural organic matter (NOM) to form I-DBPs[20, 36, 37]. UPLC-MS/MS analysis also confirmed that new byproducts were nondetectable after the addition of humic acid in the solar/IO_4^- system (**Supplementary Fig. 8**). This indicates that the solar/IO_4^- AOP is an efficient technology for 6PPD-quinone degradation without any I-DBPs formation.

$$IO_4^- \xrightarrow{UV} IO_3^{\bullet} + O^{\bullet-} \quad (1)$$

$$O^{\bullet-} + H^+ \rightarrow {}^{\bullet}OH \quad (2)$$

$$IO_4^- + O_2 + 2OH^- \xrightarrow{UV} IO_3^- + 2{}^{\bullet}O_2^- + H_2O \quad (3)$$

For the electron paramagnetic resonance (EPR) analysis on ROS identification, after adding the radical trapping agent 5,5-dimethyl-1-pyrroline N-oxide (DMPO) in dimethyl

sulfoxide (DMSO), the DMPO-$IO_3^{\bullet}$ peak (A_N = 14.6 G, A_H = 12.2 G) was readily detected (**Fig. 3c**). Meanwhile, $^{\bullet}O_2^-$ was also detected in DMSO solution, presenting in protonated form ($^{\bullet}OOH$, $^{\bullet}O_2^- + H^+ \leftrightharpoons {}^{\bullet}OOH$) with A_N = 13.7 G, A_H = 8.5 G and A_H = 1.0 G. The signal of DMPO-$IO_3^{\bullet}$ disappeared after the addition of phenol, further confirming its quenching effect for $IO_3^{\bullet}$. Moreover, in water matrix, only a weak DMPO-$^{\bullet}OH$ signal was observed with peak intensity of 1:2:2:1 ($A_N = A_H$ = 15.0 G) (**Fig. 3d and Supplementary Fig. 9**). This is because $^{\bullet}OH$ was generated by the protonation of $O^{\bullet-}$ (1.0×10^8 s^{-1}) (**Equation 2**) and the transformation reaction between $O^{\bullet-}$ and H_2O (1.8×10^6 L mol^{-1} s^{-1})[38]. The lower signal intensity was assigned to the consumption of generated IO_3^- (1.3×10^9 L mol^{-1} s^{-1}). Using nitrobenzene (NB) as a radical probe[29], we further determined the steady-state concentration of $^{\bullet}OH$ in the system as having an extremely low value of 6.4×10^{-14} mol L^{-1} (**Supplementary Fig. 10a**). Based on 6PPD-quinone degradation kinetics in the UV/H_2O_2 system (**Supplementary Fig. 10b**), the apparent second-order rate constant (k_{OP}) of $^{\bullet}OH$ with 6PPD-quinone was calculated to be 4.8×10^8 L mol^{-1} s^{-1}. The steady-state concentration of $IO_3^{\bullet}$ was determined to be 4.7×10^{-12} mol L^{-1} (**Supplementary Figs. 10c-10d**), and so the apparent second-order rate constant of $IO_3^{\bullet}$ with 6PPD-quinone was 3.0×10^{10} L mol^{-1} s^{-1}, two orders higher than for $^{\bullet}OH$.

Degradation pathway of 6PPD-quinone in solar/IO_4^- system

Compared with the structure of 6PPD, detoxification is closely related to destruction of the quinone structure of 6PPD-quinone (**Supplementary Fig. 11**)[12, 13, 32]. **Supplementary Table 3** and **Supplementary Fig. 12** present the information of primary TPs during 6PPD-quinone degradation detected by UPLC-MS/MS. Thus, **Fig. 4a** summarizes the degradation pathway of 6PPD-quinone in the solar/IO_4^- system. To break the quinone group of 6PPD-quinone at the initial degradation stage, the reaction mainly proceeded through ring-opening and C–N bond cleavage (**Fig. 4a**). Specifically, radical (mainly $IO_3^{\bullet}$) attack on 3C (Pathway I) and 6C

(Pathway II) sites led to hydroxylation of the quinone group and formation of ring-opening TPs (TP-A and TP-B) (**Supplementary Figs. 12a-12b**). Further radical attack on TP-A resulted in oxidation of the ketone group and C–N cleavage at the 9N site, causing formation of TP-G and TP-J. Then, small-molecule amino compound (TP-D, aniline) was generated after further oxidation. The formation of TP-B was mainly attributed to the ring-opening reaction at the 6C site, which was a dicarboxylic acid compound. Next, an important degradation product (TP-E) formed through pathway II, which was detected at both positive and negative modes (**Supplementary Fig. 12e** and **Fig. 12i**). Afterwards, short-chain amino fatty acids such as TP-K (amino malonic acid) were identified during the deep oxidation stage. Meanwhile, TP-C, TP-F and TP-H were saturated alkane carbon chain products generated from the parent 6PPD-quinone, after cleavage of 2C–16N and 2C–3C bonds.

Variation in mass abundance change indicated the continuous formation of TPs during the reaction (**Supplementary Fig. 13**). Specifically, TP-B first accumulated and then decomposed within the reaction time. TP-C (1,3-dimethyl butylamine) and TP-D (aniline) were directly produced after the radical attack on the 16N and 9N sites of 6PPD-quinone and intermediates, respectively (**Supplementary Figs. 12c-12d**). Using standard chemicals (**Supplementary Fig. 14**), the concentrations of TP-C and TP-D during reaction were precisely determined as 0.07 and 0.10 μmol L^{-1} at 60 min, respectively (**Supplementary Fig. 15**). Thus, the transformation rates of TP-C and TP-D from 6PPD-quinone were calculated as 21.2% and 30.0% at 60 min. TP-F was also produced through hydroxylation of the amine group after either radical addition of $^{\bullet}OH$ or hydrolysis reaction under attack by $IO_3^{\bullet}$. It is therefore suggested that $IO_3^{\bullet}$ exhibited high selectivity regarding the degradation of 6PPD-quinone and formation of TPs.

Reaction mechanism and routes of $IO_3^{\bullet}$/$^{\bullet}OH$ with 6PPD-quinone

The electrostatic potential (ESP) distribution displays the electron-rich region of 6PPD-

quinone concentrates on the quinone groups (**Fig. 5a**), which are reactive for attack by electrophiles such as $IO_3^{\bullet}$ and $^{\bullet}OH$[39]. Both the highest occupied molecular orbital (HOMO) and the lowest unoccupied molecular orbital (LUMO) of 6PPD-quinone are located in the quinone groups (**Fig. 5b**), indicating that the quinone groups exhibit high reactivity in terms of both losing and gaining electrons. The condensed Fukui index is introduced to further quantitively describe the reactive sites[40]. As both $IO_3^{\bullet}$ (primary radical) and $^{\bullet}OH$ are electrophilic species[41, 42], the electrophilicity index (ω), defined as the ability to attack the electrophilic site of target pollutants, is calculated as a measure of electrophilic power[43]. Here $IO_3^{\bullet}$ (ω = 8.11 eV) has even higher electrophilicity than $^{\bullet}OH$ (ω = 7.48 eV) (**Supplementary Fig. 16)**. In addition, theoretical calculation for $IO_3^{\bullet}$ shows that it has higher electron affinity (4.3 eV) than $^{\bullet}OH$ (1.8 eV), indicating stronger ability to achieve single electron transfer[44]. Higher values of electrophilicity index and electron affinity of $IO_3^{\bullet}$ are obtained because this radical displays a pyramidal equilibrium structure (C_{3v} symmetry), and the unpaired electron density is delocalized equally on the three oxygen atoms (**Fig. 5d**), thus elevating both the delocalized charge density and spin-orbit splitting effect[45]. Hence, the condensed Fukui index (f^-) representing the electrophilic attack on 6PPD-quinone is calculated (**Fig. 5c)**, indicating that 3C (f^- = 0.134), 6C (f^- = 0.174), 9N (f^- = 0.105), 13C (f^- = 0.085) and 16N (f^- = 0.092) sites with highest Fukui indexes are the most reactive sites. In general, the reaction routes between radicals and organic pollutants include typical RAF, HAA, and SET routes[42]. To further reveal the reactive mechanism of $IO_3^{\bullet}$ with 6PPD-quinone, especially the cleavage of quinone groups, the energy change profiles of each route are calculated. **Supplementary Tables 4-5** list the optimized structures of the reactants (R), transition state (TS) and intermediate (IM) during 6PPD-quinone oxidation determined using Gaussian software.

For the RAF route, the 3C (f^- = 0.134) and 6C (f^- = 0.174) atoms in the quinone structure with the highest electrophilic Fukui index and double bond are inclined to be attacked. However,

the energy changes indicate that RAF reaction is both thermodynamically and kinetically unfavorable at these two sites for $IO_3^{\bullet}$, owing to the positive Gibbs free energy change (ΔG = 3.4 kcal mol^{-1} at 3C and ΔG = 5.1 kcal mol^{-1} at 6C) and high reaction activation energy ($\Delta G^{\ddagger}$ = 13.7 kcal mol^{-1} at 3C and $\Delta G^{\ddagger}$ = 15.4 kcal mol^{-1} at 6C) (**Supplementary Fig. 17a** and **Fig. 5f**). It is because the large van der Waals radius (3.00 Å) of $IO_3^{\bullet}$ leads to high steric hindrance which affects the radical addition reaction. By comparison, reaction driven by $^{\bullet}OH$ with a smaller van der Waals radius (2.22 Å) is feasible thermodynamically because the RAF reactions at the 3C and 6C sites exhibit negative Gibbs free energy change (ΔG = -24.4 kcal mol^{-1} at 3C and ΔG = -16.3 kcal mol^{-1} at 6C) and low reaction energy barrier ($\Delta G^{\ddagger}$ = 5.5 kcal mol^{-1} at 3C and $\Delta G^{\ddagger}$ = 6.7 kcal mol^{-1} at 6C). The addition product of $^{\bullet}OH$ then achieves cleavage of the C–N bond (2C–16N and 4C–9N) (**Fig. 4b**). Moreover, $^{\bullet}OH$ addition at the 3C site leads to formation of TP-C after electron transfer between fragments and the hydrolysis reaction, whereas addition at the 6C site leads to the formation of TP-D (**Fig. 4b**). However, the contribution of the RAF route driven by $^{\bullet}OH$ to 6PPD-quinone is limited as previously discussed, due to the low concentration of generated $^{\bullet}OH$. This unfavorable RAF route for $IO_3^{\bullet}$ avoids generation of iodine-addition byproducts, consistent with the TPs identified by UPLC-MS/MS (**Fig. 4a**).

$$6PPD-quinone + IO_3^{\bullet} \xrightarrow{HAA} 6PPD-quinone^{\bullet} + HIO_3 \quad (4)$$

$$6PPD-quinone + {}^{\bullet}OH \xrightarrow{HAA} 6PPD-quinone^{\bullet} + H_2O \quad (5)$$

For the HAA route, 6PPD-quinone transforms into a neutral carbon-centered radical (6PPD-quinone$^{\bullet}$) after H abstraction, and meanwhile, $IO_3^{\bullet}$ and $^{\bullet}OH$ transform into HIO_3 and H_2O (**Equations 4-5**) (**Supplementary Fig. 18**)[46]. In addition, abstraction of H atoms in the quinone structure (C3–23H and C6–24H) and associated with N (N9–H25 and N16–H31) are likely to occur due to the low values of bond dissociation energy (BDE), which is of considerable relevance to the toxic quinone structure (**Supplementary Table 6**). However, the

energy changes indicate that the $IO_3^{\bullet}$-driven HAA reaction at the four sites is thermodynamically unfavorable considering the positive Gibbs free energy changes and quite high reaction activation energies (**Fig. 5f**). Conversely, for the $^{\bullet}OH$-driven HAA reaction, abstraction of H atoms at all the considered sites is thermodynamically favorable due to the negative ΔG values (**Supplementary Fig. 17c**). However, high activation energies are observed at 3C ($\Delta G^{\ddagger}$ = 7.4 kcal mol^{-1}) and 6C ($\Delta G^{\ddagger}$ = 10.6 kcal mol^{-1}) sites. Thus, the most reactive sites are located at 16N and 9N due to the greatly negative ΔG and lower $\Delta G^{\ddagger}$ (**Fig. 5f**). We now introduce bond order as a descriptor to describe bonding strength in order to investigate the bond change during the reaction (**Supplementary Tables 7-8**)[42]. The bond order of 9N–25H gradually decreases from 0.74 for R to 0.53 for TS, and then to 0.17 for IM, while the bond order of 25H–46O increases from 0.22 (R) to 0.82 (IM) (**Supplementary Table 7**), implying cleavage of the 9N–25H bond in 6PPD-quinone and formation of 25H–46O bond in the H_2O molecule. The spin density distribution also exhibits spin change from the 46O atom of $^{\bullet}OH$ to the 9N site of 6PPD-quinone during HAA process by $^{\bullet}OH$ (**Fig. 5e).** A similar result is also obtained at the 16N–31H site (**Supplementary Table 8**). The HAA route driven by $^{\bullet}OH$ at the 16N and 9N sites leads to the generation of N-centered radicals (**Supplementary Fig. 19**). Then, C–N cleavage occurs through subsequent electron transfer from the 3C/6C sites on the quinone structure, resulting in the formation of TP-C and TP-D (**Fig. 4c**).

Single electron transfer mechanism from 6PPD-quinone to $IO_3^{\bullet}$

During the SET process, electrons transfer from 6PPD-quinone molecules to oxidant ($IO_3^{\bullet}$ and $^{\bullet}OH$) (**Equations 6–7**), leading to the formation of 6PPD-quinone$^{\bullet+}$ (**Fig. 4d**), after which a series of subsequent reactions occur. The energy change profile indicates that the SET reaction driven by $^{\bullet}OH$ for 6PPD-quinone oxidation is thermodynamically unfavorable (ΔG = 10.4 kcal mol^{-1}), with a high energy barrier of $\Delta G^{\ddagger}$ = 22.6 kcal mol^{-1} (**Fig. 5f**). However, for $IO_3^{\bullet}$, a

negative ΔG (-28.3 kcal mol^{-1}) and a low $\Delta G^{\ddagger}$ value of 4.5 kcal mol^{-1} are obtained, suggesting that this reaction is both thermodynamically and kinetically favorable. As discussed earlier, $IO_3^{\bullet}$ plays the dominant role in 6PPD-quinone degradation, but $IO_3^{\bullet}$ cannot react with this pollutant through RAF and HAA routes, and so SET is the primary reaction route. $IO_3^{\bullet}$ readily gains electrons from the 6PPD-quinone molecule, owing to the very negative energy of the lowest unoccupied molecular orbital (ELUMO). The calculated ELUMOs of $IO_3^{\bullet}$ and $^{\bullet}OH$ are -6.7 and -4.9 eV, respectively (**Supplementary Fig. 20**). Therefore, $IO_3^{\bullet}$ can accept electrons from 6PPD-quinone due to the more negative energy level, but $^{\bullet}OH$ cannot. Moreover, a dipole moment is created as $IO_3^{\bullet}$ approaches the 6PPD-quinone molecules (**Fig. 5d**), requiring self-driven electron transfers to maintain spatial inversion symmetry. The SET process mainly occurs at the 3C and 6C sites in the quinone structure of 6PPD-quinone, due to the higher electrophilic Fukui index and uneven electron density of the conjugated π orbital of the C=C bond (**Fig. 5c**). We now take the 6C site as an example for further discussion noting that it has the highest Fukui index (f^- = 0.174) and largest spin density (0.392) after losing an electron (**Supplementary Table 9**).

$$6PPD-quinone + IO_3^{\bullet} \xrightarrow{SET} 6PPD-quinone^{\bullet+} + IO_3^- \quad (6)$$

$$6PPD-quinone + {}^{\bullet}OH \xrightarrow{SET} 6PPD-quinone^{\bullet+} + OH^- \quad (7)$$

The SOMOs of $IO_3^{\bullet}$ and 6PPD-quinone are further analyzed to explore the electron transfer process at the molecular orbital level (**Fig. 6a**). For $IO_3^{\bullet}$, the I–O bond has a sp^3-hybridization form, where the unpaired electron is distributed on the non-bonding (n) orbital. Both O and I atoms in the I–O bond have delocalized electron pairs, with the empty antibonding orbital of the I=O double bond available for effective promotion of charge transfer[22]. For 6PPD-quinone, the conjugated π electron between the two ketone groups and the connected asymmetric amino groups results in uneven electron density inside the molecule. For the most reactive 6C site for SET reaction, sp^2-hybridization is adopted for the 5C=6C double bond,

including three σ orbitals and one π orbital. The π electron with higher reactivity tends to be captured by $IO_3^{\bullet}$ and enters the n orbital of $IO_3^{\bullet}$, forming IO_3^- and 6PPD-quinone$^{\bullet+}$. The isosurface of charge density difference also shows the generation of electron-rich and electron-deficient regions on the quinone structure after electron transfer from 6PPD-quinone to $IO_3^{\bullet}$ (**Supplementary Fig. 21**). The charge transfer characteristic of π electron involvement is obtained from the output configuration information, attributed to the nodal isosurface on the conjugate plane.

6PPD-quinone$^{\bullet+}$ generated from the SET reaction by $IO_3^{\bullet}$ is the key species for further reaction, as ring-opening reaction can be achieved through hydrolysis of 6PPD-quinone$^{\bullet+}$ (**Fig. 4d**), leading to destruction of quinone structure and toxicity attenuation. Spin density distribution analysis shows that unpaired electrons of 6PPD-quinone$^{\bullet+}$ mainly concentrate on 6C (0.392) and 3C (0.266) atoms (**Fig. 6b**), where the radical electron delocalizes on the ring of the quinone structure causing resonance and promoting the hydrolysis reaction. In the hydrolysis process (**Fig. 4d**), 6PPD-quinone$^{\bullet+}$ is attacked by H_2O molecules and a ring-opening radical (TP-RO) forms after charge rearrangement-induced cleavage of the 6C–5C bond. Later, a radical coupling reaction occurs between TP-RO and $IO_3^{\bullet}$, resulting in a precursor of the detected TP-B product (TP-PB) after charge transfer between fragments. Similarly, the $IO_3^{\bullet}$-driven SET reaction occurs at the 3C site, leading to production of the precursor of TB-A (TP-PA) (**Supplementary Fig. 22**). After further oxidation, TP-PA and TP-PB transform into TP-C and TP-D, confirmed to be the primary TPs in the solar/IO_4^- system.

We further confirmed the production of 6PPD-quinone$^{\bullet+}$ through EPR and femtosecond transient absorption spectra (fs-TAS) measurement. In the EPR test, the generated 6PPD-quinone$^{\bullet+}$ was captured by DMPO at a lower temperature (275 K), with a characteristic signal of A_N = 16.4 G and A_H = 23.2 G (**Fig. 6c**). The radical signal with a total spectral width of 56 G and A_H/A_N ratio of 1.4 was assigned to a saturated carbon-centered radical[47]. In addition,

before fs-TAS characterization, the theoretical UV-vis light absorption spectra of 6PPD-quinone and 6PPD-quinone$^{\bullet+}$ are simulated through a time-dependent density functional theory (TDDFT) calculation (**Supplementary Fig. 23**). Compared to 6PPD-quinone, the main absorption peak of 6PPD-quinone$^{\bullet+}$ displays a red shift from 340 to 360 nm after electron transfer. Moreover, an emerging peak at 550−700 nm is also observed, as a characteristic absorption signal for 6PPD-quinone$^{\bullet+}$. The fs-TAS detection then confirmed the formation process of 6PPD-quinone$^{\bullet+}$ because of the broad negative peak observed at 550−700 nm corresponding to the signal of ground-state bleach (GSB) (**Fig. 6d**)[48]. The GSB signals were attributed to the generation of the excited state, which was more reactive for oxidation. Interestingly, the bleach signal exhibited a red shift from 600 to 635 nm with reaction time, implying the effectiveness of electron transfers among the quinone structure and the excited-state geometric relaxation[49]. The shift of the main peak therefore explains the simultaneous reaction between generation and oxidation processes of 6PPD-quinone$^{\bullet+}$. In addition, dynamics of the GSB signal indicate the fast speed of the electron transfer process as signals were observed just in 5 ps (**Supplementary Fig. 24**)[50]. In summary, the generation of 6PPD-quinone$^{\bullet+}$ was found to be the most important transformation intermediate in the SET reaction, with the ring-opening reaction of the quinone structure achieved under $IO_3^{\bullet}$ attack.

Water chemistry factors effects and 6PPD-quinone degradation under natural solar light. To verify the applicability of solar/IO_4^- system to the degradation of 6PPD-quinone in actual aquatic environments, the effects of various water chemical factors were investigated. Our results indicate that high 6PPD-quinone degradation efficiencies were obtained over a wide pH range of 3–9 (> 88%) (**Supplementary Fig. 25a**). In addition, in the presence of a high concentration of Na^+ (1.0 mmol L^{-1}), Ca^{2+} (1.0 mmol L^{-1}), Cl^- (1.0 mmol L^{-1}) and HA (1.0 mg L^{-1} as TOC), the final concentration of 6PPD-quinone was still below 1 μg L^{-1} after 60-min reaction, achieving high degradation efficiencies of > 99% (**Supplementary Figs. 25b-25c**).

In real water matrixes such as lake and river water bodies (**Supplementary Fig. 25d**), the 6PPD-quinone degradation efficiency was inhibited due to the radical quenching effects caused by natural organic matter and microorganisms. However, solar/IO_4^- system still showed better performance than solar/H_2O_2 and solar/PDS systems. To verify the effectiveness of 6PPD-quinone degradation by IO_4^- activated under natural solar light, experiments were carried out at times of 10:00 (light intensity = 45 mW cm^{-2}), 13:00 (light intensity = 60 mW cm^{-2}) and 16:00 (light intensity = 18 mW cm^{-2}), respectively (**Supplementary Fig. 26**). Photolysis of 6PPD-quinone hardly occurred under natural solar light (**Fig. 2d**). However, in the 10:00 and 13:00 tests with the addition of IO_4^-, 6PPD-quinone was degraded by 94.0% and 94.8% within 60 min, and the residual concentrations were below 1 μg L^{-1}. The foregoing results indicate that the solar/IO_4^- system can efficiently degrade environmental-level 6PPD-quinone under natural solar light.

Implications for 6PPD-quinone degradation research

The emerging threat of 6PPD-quinone to the natural water environment is greatly concerning due to the sheer quantity of tire-wear particles in urban rainwater runoff and water bodies. For the removal of 6PPD-quinone from water, efficient and effective technologies, such as AOPs with high reactive species, urgently require implementation in order to remove this contaminant from water even at environment-level concentration. The present study has reported on a solar-light-driven periodate activation system that achieves removal of 6PPD-quinone at environmental level with high efficiency (> 99%), resulting in a residual concentration much lower than the reported LC_{50} for coho salmon (an aquatic organism that is highly sensitive to 6PPD-quinone). More importantly, as a specific, key reactive species, $IO_3^{\bullet}$ is found to exhibit higher electrophilicity and electronic affinity than conventional $^{\bullet}OH$. The underlying mechanisms of $IO_3^{\bullet}$-driven SET reaction and quinone structure ring-opening reaction for

detoxification have been explored at the molecular level. In short, the IO_4^- activation system effectively removes 6PPD-quinone under conditions of natural solar light with strong environmental resistance, providing a reference technology for the treatment and removal of toxic organic pollutants from water.

Methods

6PPD-quinone degradation by IO_4^- activated under solar light

Batch degradation experiments were carried out in a quartz reactor with circulating water to maintain the temperature at 25 °C. Simulated solar light was supplied by Microsolar 300A irradiation equipment (AM1.5 mode, Beijing PerfectLight, China) equipped with a 300 W Xe light, whose light intensity was set at 100 mW cm^{-2} during the solar irradiation process. A typical 6PPD-quinone degradation test was carried out as follows: 99 mL of 6PPD-quinone (100 μg L^{-1}) and 1 mL of 20 mmol L^{-1} IO_4^- (stock solution concentration of 20 mmol L^{-1}) were mixed and stirred at 400 rpm. The solution pH was adjusted to 5 using $HClO_4$ and NaOH (0.1 mmol L^{-1}). IO_4^- activation was initialized after the simulated solar light was switched on. At predetermined time intervals, a 1 mL sample was collected immediately in a vial, and 10 μL of 0.1 mol L^{-1} $Na_2S_2O_3$ pre-injected into the vial to quench the radical reaction. All experiments were conducted in triplicate. Control tests of photolysis and direct oxidation of IO_4^- were also carried out under the same conditions. Degradation experiments under natural sunlight irradiation were performed outdoors in August 2022 on the campus of Peking University (Longitude: 116.31088; latitude: 39.99281), Beijing, China. Degradation experiments were carried out at 10:00, 13:00 and 16:00, when the light intensity was ~45, 60 and 18 mW cm^{-2} measured by an optical power meter (1919-R, Newport), respectively. The quantum yield of IO_4^- was calculated from the fluence-based reaction rate constants[29, 51].

Analysis of 6PPD-quinone and formed I-related species

Concentration of 6PPD-quinone was determined using a UPLC-MS/MS (Dionex UltiMate 3000 Series; MS, Thermo Scientific, USA) equipped with a Zorbax RX-C18 column. The column temperature was set at 30 ℃ and a sample volume of 5 μL injected. The mobile phase comprised a mixture of chromatography-grade water with 0.1% formic acid and methanol at a flow rate of 0.2 mL min^{-1}. Concentrations of IO_4^-, IO_3^-, HOI and I^- were determined by UPLC-MS/MS in electrospray ionization negative mode (ESI^- mode). The concentration of I_2 was determined by measuring the absorbance at 460 nm[36].

Zebrafish exposure test on toxicity evaluation

Zebrafish eggs were collected from adult zebrafish, maintained in an automatic circulation system at 28 °C and subject to a regular light (14 h)/dark (10 h) cycle. Exposure tests were conducted using 12 well plates with 15 embryos per well in a constant temperature incubator at 28 °C, following the Organization for Economic Cooperation and Development (OECD) test guideline (236) for fish embryo acute toxicity[52]. The embryos were exposed to water samples (containing residual 6PPD-quinone and TPs) taken at predetermined degradation time intervals (0–120 min) for 48 hours post-fertilization (hpf). The exposure tests were conducted in triplicate and 15 embryos were used in each parallel experiment (*i.e.*, a total of 45 embryos for each collected water sample). Embryo pictures were obtained by means of an inverted biomicroscope (JSZ6S, Olympus, Japan). Mortality rate and hatching rate were recorded.

EPR test on the identification of radicals

ROS generated in the solar/IO_4^- AOP system was obtained using an EMXplus-6/1 EPR spectrometer (Bruker, Germany). DMPO was used as a spin-trapping agent for the detection of $^{\bullet}OH$, $^{\bullet}O_2^-$ and $IO_3^{\bullet}$ in the reaction system in water or DMSO. Specifically, the mixture for $^{\bullet}OH$ detection was prepared by mixing 50 μL of DMPO (1 mol L^{-1}) and 450 μL of IO_4^- (10 mmol L^{-1}) solution in water, whereas $^{\bullet}O_2^-$ and $IO_3^{\bullet}$ were detected in DMSO. The resulting EPR data

were analyzed using MATLAB Software (version R2021a) and the EasySpin package (version 5.2.33).

DFT calculation methods

Theoretical calculations of the 6PPD-quinone reaction are all performed by Gaussian 16 C.01 software[53]. All geometrical optimization and vibrational frequencies of R, TS and IM are calculated using hybrid density functional theory (DFT) at B3LYP/def-SVP level. Single-point energy, spin density, and electrophilicity index of radicals and organic compounds are calculated for the optimized geometry using B3LYP/def2-TZVP. Specific analysis is completed by Multiwfn 3.8 software, combined with Visual Molecular Dynamics (VMD) software[54]. The change in Gibbs free energy of reaction (ΔG, kcal mol^{-1}) is determined as the difference between the product and reactant of elementary processes, while the reaction activation energy ($\Delta G^{\ddagger}$, kcal mol^{-1}) is calculated as the difference between TS and R for HAA and RAF routes. Electrostatic potential, HOMO, LUMO, condensed Fukui index of 6PPD-quinone, and BDE of the H–C/H–N bond are calculated at B3LYP/def-TZVP level after geometrical optimization of the chemical structure. Theoretical UV-vis absorption spectra are obtained by calculating the excited states using time-dependent density functional theory (TDDFT). Sixty excited states are evaluated in the TDDFT calculation to cover the entire UV-visible light range.

Data availability

All relevant data that support the findings of this study are presented in the Article and Supplementary Information. Source data are provided in this paper. The source data can also be accessed through the fig-share repository and are freely available for download.

Code availability

The codes for structural optimization of organic compounds performed on Gaussian 16 software are provided in this paper. The initial configuration of reactants and conjectured

structure of the transition state (TS) is built on GaussView. The geometrical optimization and vibrational frequency are calculated at the B3LYP/def-SVP level. Single-point energy, spin density, charge distribution, and electrophilicity index are calculated for the optimized geometry at the B3LYP/def2-TZVP level. Specific analysis is completed by Multiwfn 3.8 software, combined with Visual Molecular Dynamics (VMD) software.

Acknowledgements

We thank the National Natural Science Foundation of China (NSFC) (52270053 (W.L.)), the National Key Research and Development Program of China (2021YFA1202500 (W.L.)), the Beijing Natural Science Foundation (No. 8232035(W.L.)) and the Beijing Nova Program (20220484215 (W.L.)) for financial support. The High-Performance Computing Platform of Peking University is also greatly acknowledged for DFT calculations support.

Author contributions

L.C. and W. L. conceived the idea and designed the research. L.C., J.R.H. and D.T.J. performed the experiment including degradation kinetics, transformation products detection, radical detection and Zebrafish exposure tests. L.C. and H.X.Z. performed the DFT calculations. A.G.L.B. and W.L.S. provided constructive suggestions for the results and discussion. L.C., W.L. and A.G.L.B. contributed to writing the manuscript. All coauthors discussed the results.

Competing interests

The authors declare no competing interests.

Additional information

Supplementary information

The online version contains supplementary material available at XXX.

Figure Legends

Fig. 1 Schematic diagram showing the construction of the periodate activation system for

degradation of 6PPD-quinone. a, Transformation route from 6PPD to 6PPD-quinone through ozonation in the environment. **b,** Design of solar-light-driven periodate activation system and properties of generated $IO_3^{\bullet}$. **c,** Degradation of 6PPD-quinone under attack from $IO_3^{\bullet}$ and $^{\bullet}OH$.

Fig. 2 Degradation and toxicity reduction of 6PPD-quinone by solar light activating periodate. a, Degradation kinetics of 6PPD-quinone in the solar/IO_4^- system. **b,** Degradation kinetics of 6PPD-quinone in solar/IO_4^-, solar/PDS and solar/H_2O_2 systems. **c,** Acute mortality of zebrafish (48 h) after addition of degradation water samples in the solar/IO_4^- system at predetermined time intervals. **d,** Degradation performance of 6PPD-quinone under natural solar light. Data are presented as mean values ± standard deviation from triplicate independent experiments (n = 3). Experimental conditions: pH = 5, [oxidant (IO_4^-, PDS or H_2O_2)] = 0.2 mmol L^{-1}; [6PPD-quinone] = 100, 50, or 10 μg L^{-1} for **a**, [6PPD] = 100 μg L^{-1} for **b-d**.

Fig. 3 The contribution and identification of reactive species on the degradation of 6PPD-quinone in the solar/IO_4^- system. a, Influence of different scavengers on 6PPD-quinone degradation. **b,** Conversion of iodine-related species during the reaction. **c,** EPR spectra of DMPO-$^{\bullet}OOH$ and DMPO-$IO_3^{\bullet}$ in DMSO (SSL: simulated solar light). **d,** EPR spectra of DMPO-$^{\bullet}OH$ and DMPOO in water. Data in **a** and **b** are presented as mean values ± standard deviation from triplicate independent experiments (n = 3). Experimental conditions: pH = 5, [IO_4^-] = 0.2 mmol L^{-1}, [6PPD-quinone] = 100 μg L^{-1}; [scavenger] = 50 mmol L^{-1} for **a**, [DMPO] = 100 mmol L^{-1} for **c** and **d**.

Fig. 4 Degradation pathway of 6PPD-quinone and typical initial reaction for destruction of quinone structure. a, Proposed degradation pathway of 6PPD-quinone in the solar/IO_4^- system. **b,** Radical adduct formation route for $^{\bullet}OH$. **c,** Hydrogen atom abstraction route for $IO_3^{\bullet}$ and $^{\bullet}OH$. **d,** Single electron transfer reaction for $IO_3^{\bullet}$.

Fig. 5 Reactive sites of electrophilic attack and energy change for HAA and SET routes. **a**, ESP distribution of 6PPD-quinone. **b**, HOMO and LUMO distributions of 6PPD-quinone. **c,**

Natural population analysis (NPA) of charge distribution (q) and condensed Fukui index (f^-) representing electrophilic attack on 6PPD-quinone. **d,** Spin densities of $^{\bullet}OH$ and $IO_3^{\bullet}$. **e,** Spin density distribution of reactants (R), transition states (TS), and intermediates (IM) during 6PPD-quinone degradation through HAA reaction at 9N site by $^{\bullet}OH$. **f,** Hot map of Gibbs free energy change (ΔG) and reaction activation energy ($\Delta G^{\ddagger}$) for typical reaction routes.

Fig. 6 Single electron transfer mechanism from 6PPD-quinone to $IO_3^{\bullet}$. a, SET reaction mechanism for 6PPD-quinone oxidation by $IO_3^{\bullet}$ at 6C site based on dynamic analysis of the electron distribution at the molecular orbital level. **b,** Calculated spin density of 6PPD-quinone and 6PPD-quinone$^{\bullet+}$. **c,** EPR spectra of detected 6PPD-quinone cationic radical. **d,** Femtosecond transient absorption spectra (fs-TAS) of 6PPD-quinone$^{\bullet+}$ in the time range of the IO_4^- activation system (λ_{exc} = 320 nm).

References

1. Hu, X., Zhao, H.N., Tian, Z., Peter, K.T., Dodd, M.C., Kolodziej, E.P. Transformation product formation upon heterogeneous ozonation of the tire rubber antioxidant 6PPD (N-(1,3-dimethylbutyl)-N′-phenyl-p-phenylenediamine). *Environ. Sci. Technol. Lett.* **9**, 413-419 (2022).
2. Ziajahromi, S., Lu, H.-C., Drapper, D., Hornbuckle, A., Leusch, F.D.L. Microplastics and tire wear particles in urban stormwater: Abundance, characteristics, and potential mitigation strategies. *Environ. Sci. Technol.* **57**, 12829-12837 (2023).
3. Seiwert, B., Nihemaiti, M., Troussier, M., Weyrauch, S., Reemtsma, T. Abiotic oxidative transformation of 6-PPD and 6-PPD quinone from tires and occurrence of their products in snow from urban roads and in municipal wastewater. *Water Res.* **212**, 118122 (2022).
4. Zhao, H.N., *et al.* Screening p-phenylenediamine antioxidants, their transformation products, and industrial chemical additives in crumb rubber and elastomeric consumer products. *Environ. Sci. Technol.* **57**, 2779-2791 (2023).
5. Hiki, K., *et al.* Acute toxicity of a tire rubber-derived chemical, 6PPD quinone, to

freshwater fish and crustacean species. *Environ. Sci. Technol. Lett.* **8**, 779-784 (2021).

6. Zoroufchi Benis, K., Behnami, A., Minaei, S., Brinkmann, M., McPhedran, K.N., Soltan, J. Environmental occurrence and toxicity of 6PPD quinone, an emerging tire rubber-derived chemical: A review. *Environ. Sci. Technol. Lett.* **10**, 815-823 (2023).

7. Rossomme, E., Hart-Cooper, W.M., Orts, W.J., McMahan, C.M., Head-Gordon, M. Computational studies of rubber ozonation explain the effectiveness of 6PPD as an antidegradant and the mechanism of its quinone formation. *Environ. Sci. Technol.* **57**, 5216-5230 (2023).

8. Li, C.*, et al.* First insights into 6PPD-quinone formation from 6PPD photodegradation in water environment. *J. Hazard. Mater.* **459**, 132127 (2023).

9. Zhou, Y.*, et al.* Sunlight-induced transformation of tire rubber antioxidant N-(1,3-dimethylbutyl)-N′-phenyl-p-phenylenediamine (6PPD) to 6PPD-quinone in water. *Environ. Sci. Technol. Lett.* **10**, 798-803 (2023).

10. Tian, Z.*, et al.* A ubiquitous tire rubber–derived chemical induces acute mortality in coho salmon. *Science* **371**, 185-189 (2021).

11. Zhang, Y.-J., Xu, T.-T., Ye, D.-M., Lin, Z.-Z., Wang, F., Guo, Y. Widespread N-(1,3-dimethylbutyl)-N′-phenyl-p-phenylenediamine quinone in size-fractioned atmospheric particles and dust of different indoor environments. *Environ. Sci. Technol. Lett.* **9**, 420-425 (2022).

12. Grasse, N., Seiwert, B., Massei, R., Scholz, S., Fu, Q., Reemtsma, T. Uptake and biotransformation of the tire rubber-derived contaminants 6-PPD and 6-PPD quinone in the zebrafish embryo (*Danio rerio*). *Environ. Sci. Technol.* **57**, 15598-15607 (2023).

13. Di, S.*, et al.* Chiral perspective evaluations: Enantioselective hydrolysis of 6PPD and 6PPD-quinone in water and enantioselective toxicity to *Gobiocypris rarus* and *Oncorhynchus mykiss*. *Environ. Int.* **166**, 107374 (2022).

14. Tian, Z.Y.*, et al.* 6PPD-quinone: Revised toxicity assessment and quantification with a commercial standard. *Environ. Sci. Technol. Lett.* **9**, 140-146 (2022).

15. Cao, G.*, et al.* New evidence of rubber-derived quinones in water, air, and soil. *Environ. Sci. Technol.* **56**, 4142-4150 (2022).

16. Yin, R., Anderson, C.E., Zhao, J., Boehm, A.B., Mitch, W.A. Controlling contaminants

using a far-UVC-based advanced oxidation process for potable reuse. *Nat. Water* **1**, 555-562 (2023).

17. Zhang, D., Li, Y., Wang, P., Qu, J., Li, Y., Zhan, S. Dynamic active-site induced by host-guest interactions boost the Fenton-like reaction for organic wastewater treatment. *Nat. Commun.* **14**, 3538 (2023).

18. Liu, F.*, et al.* Catalyst-free periodate activation by solar irradiation for bacterial disinfection: Performance and mechanisms. *Environ. Sci. Technol.* **56**, 4413-4424 (2022).

19. Kim, Y.*, et al.* Revisiting the oxidizing capacity of the periodate–H_2O_2 mixture: Identification of the primary oxidants and their formation mechanisms. *Environ. Sci. Technol.* **56**, 5763-5774 (2022).

20. Sun, H., He, F., Choi, W. Production of reactive oxygen species by the reaction of periodate and hydroxylamine for rapid removal of organic pollutants and waterborne bacteria. *Environ. Sci. Technol.* **54**, 6427-6437 (2020).

21. Zong, Y.*, et al.* Surface-mediated periodate activation by nano zero-valent iron for the enhanced abatement of organic contaminants. *J. Hazard. Mater.* **423**, 126991 (2022).

22. Wen, H., Hou, G.-L., Huang, W., Govind, N., Wang, X.-B. Photoelectron spectroscopy of higher bromine and iodine oxide anions: Electron affinities and electronic structures of $BrO_{2,3}$ and IO_{2-4} radicals. *J. Chem. Phys.* **135**, 184309 (2011).

23. Du, P.H., Wang, J.J., Sun, G.D., Chen, L., Liu, W. Hydrogen atom abstraction mechanism for organic compound oxidation by acetylperoxyl radical in Co(II)/peracetic acid activation system. *Water Res.* **212**, 118113 (2022).

24. Zhang, N., Samanta, S.R., Rosen, B.M., Percec, V. Single electron transfer in radical ion and radical-mediated organic, materials and polymer synthesis. *Chem. Rev.* **114**, 5848-5958 (2014).

25. Hu, J.*, et al.* Animal production predominantly contributes to antibiotic profiles in the Yangtze River. *Water Res.* **242**, 120214 (2023).

26. Wu, Q.-Y., Yang, Z.-W., Wang, Z.-W., Wang, W.-L. Oxygen doping of cobalt-single-atom coordination enhances peroxymonosulfate activation and high-valent cobalt–oxo species formation. *Proc. Natl. Acad. Sci.* **120**, e2219923120 (2023).

27. Chuang, Y.-H., Wu, K.-L., Lin, W.-C., Shi, H.-J. Photolysis of chlorine dioxide under UVA irradiation: Radical formation, application in treating micropollutants, formation of disinfection byproducts, and toxicity under scenarios relevant to potable reuse and drinking water. *Environ. Sci. Technol.* **56**, 2593-2604 (2022).
28. Lee, J., von Gunten, U., Kim, J.-H. Persulfate-based advanced oxidation: Critical assessment of opportunities and roadblocks. *Environ. Sci. Technol.* **54**, 3064-3081 (2020).
29. Li, J.*, et al.* Ozone- and hydroxyl radical-induced degradation of micropollutants in a novel UVA-LED-activated periodate advanced oxidation process. *Environ. Sci. Technol.* **57**, 18607-18616 (2023).
30. Greer, J.B., Dalsky, E.M., Lane, R.F., Hansen, J.D. Tire-derived transformation product 6PPD-quinone induces mortality and transcriptionally disrupts vascular permeability pathways in developing coho salmon. *Environ. Sci. Technol.* **57**, 10940-10950 (2023).
31. Peng, W., Liu, C., Chen, D., Duan, X., Zhong, L. Exposure to N-(1,3-dimethylbutyl)-N′-phenyl-p-phenylenediamine (6PPD) affects the growth and development of zebrafish embryos/larvae. *Ecotox. Environ. Safe.* **232**, 113221 (2022).
32. Varshney, S., Gora, A.H., Siriyappagouder, P., Kiron, V., Olsvik, P.A. Toxicological effects of 6PPD and 6PPD quinone in zebrafish larvae. *J. Hazard. Mater.* **424**, 127623 (2022).
33. Zhang, S.-Y.*, et al.* 6PPD and its metabolite 6PPDQ induce different developmental toxicities and phenotypes in embryonic zebrafish. *J. Hazard. Mater.* **455**, 131601 (2023).
34. Choi, Y.*, et al.* Activation of periodate by freezing for the degradation of aqueous organic pollutants. *Environ. Sci. Technol.* **52**, 5378-5385 (2018).
35. Long, Y., Dai, J., Zhao, S., Su, Y., Wang, Z., Zhang, Z. Atomically dispersed cobalt sites on graphene as efficient periodate activators for selective organic pollutant degradation. *Environ. Sci. Technol.* **55**, 5357-5370 (2021).
36. Chen, T.*, et al.* Understanding the importance of periodate species in the pH-dependent degradation of organic contaminants in the H_2O_2/periodate process. *Environ. Sci. Technol.* **56**, 10372-10380 (2022).
37. Niu, L., Lin, J., Chen, W., Zhang, Q., Yu, X., Feng, M. Ferrate(VI)/periodate system:

630 Synergistic and rapid oxidation of micropollutants via periodate/iodate-modulated
631 Fe(IV)/Fe(V) intermediates. *Environ. Sci. Technol.* **57**, 7051-7062 (2023).
632 38. Buxton, G.V., Greenstock, C.L., Helman, W.P., Ross, A.B. Critical review of rate
633 constants for reactions of hydrated electrons, hydrogen atoms and hydroxyl radicals
634 ($^{\bullet}OH/^{\bullet}O^{-}$) in aqueous solution. *J. Phys. Chem. Ref. Data* **17**, 513-886 (1988).
635 39. Wang, Q.*, et al.* ESP–ALIE analysis as a theoretical tool for identifying the coordination
636 atoms of possible multisite extractants: Validation and prediction. *ACS Sustain. Chem.*
637 *Eng.* **8**, 14353-14364 (2020).
638 40. Li, F., Borthwick, A.G.L., Liu, W. Environmental theoretical calculation for non-
639 periodic systems. *Trends Chem.* **5**, 410-414 (2023).
640 41. Chen, L., Duan, J., Du, P.H., Sun, W.L., Lai, B., Liu, W. Accurate identification of
641 radicals by in-situ electron paramagnetic resonance in ultraviolet-based homogenous
642 advanced oxidation processes. *Water Res.* **221**, 118747 (2022).
643 42. Zhang, H., Xie, C., Chen, L., Duan, J., Li, F., Liu, W. Different reaction mechanisms of
644 $SO_4^{\bullet-}$ and $^{\bullet}OH$ with organic compound interpreted at molecular orbital level in
645 Co(II)/peroxymonosulfate catalytic activation system. *Water Res.* **229**, 119392 (2023).
646 43. De Vleeschouwer, F., Van Speybroeck, V., Waroquier, M., Geerlings, P., De Proft, F.
647 Electrophilicity and nucleophilicity index for radicals. *Org. Lett.* **9**, 2721-2724 (2007).
648 44. Rienstra-Kiracofe, J.C., Tschumper, G.S., Schaefer, H.F., Nandi, S., Ellison, G.B.
649 Atomic and molecular electron affinities: Photoelectron experiments and theoretical
650 computations. *Chem. Rev.* **102**, 231-282 (2002).
651 45. Ren, W.*, et al.* Origins of electron-transfer regime in persulfate-based nonradical
652 oxidation processes. *Environ. Sci. Technol.* **56**, 78-97 (2021).
653 46. Bím, D., Maldonado-Domínguez, M., Rulíšek, L., Srnec, M. Beyond the classical
654 thermodynamic contributions to hydrogen atom abstraction reactivity. *Proc. Natl. Acad.*
655 *Sci.* **115**, E10287-E10294 (2018).
656 47. Gao, H.-Y.*, et al.* First direct and unequivocal electron spin resonance spin-trapping
657 evidence for pH-dependent production of hydroxyl radicals from sulfate radicals.
658 *Environ. Sci. Technol.* **54**, 14046-14056 (2020).
659 48. Zeman, C.J.I.V., Kim, S., Zhang, F., Schanze, K.S. Direct observation of the reduction

of aryl halides by a photoexcited perylene diimide radical anion. *J. Am. Chem. Soc.* **142**, 2204-2207 (2020).

49. Shi, Y.A.*, et al.* Small reorganization energy acceptors enable low energy losses in non-fullerene organic solar cells. *Nat. Commun.* **13**, 3256 (2022).

50. Ponseca, C.S., Jr., Chábera, P., Uhlig, J., Persson, P., Sundström, V. Ultrafast electron dynamics in solar energy conversion. *Chem. Rev.* **117**, 10940-11024 (2017).

51. Yin, R., Ling, L., Shang, C. Wavelength-dependent chlorine photolysis and subsequent radical production using UV-LEDs as light sources. *Water Res.* **142**, 452-458 (2018).

52. OECD. Test No. 236: Fish embryo acute toxicity (FET) test, OECD guidelines for the testing of chemicals, Section 2. https://doi.org/10.1787/9789264203709-en (2013).

53. Frisch, M.*, et al.* Gaussian 16, Revision C.01. Gaussian, Inc. Wallingford, CT (2016).

54. Lu, T., Chen, F. Multiwfn: A multifunctional wavefunction analyzer. *J. Comput. Chem.* **33**, 580-592 (2012).

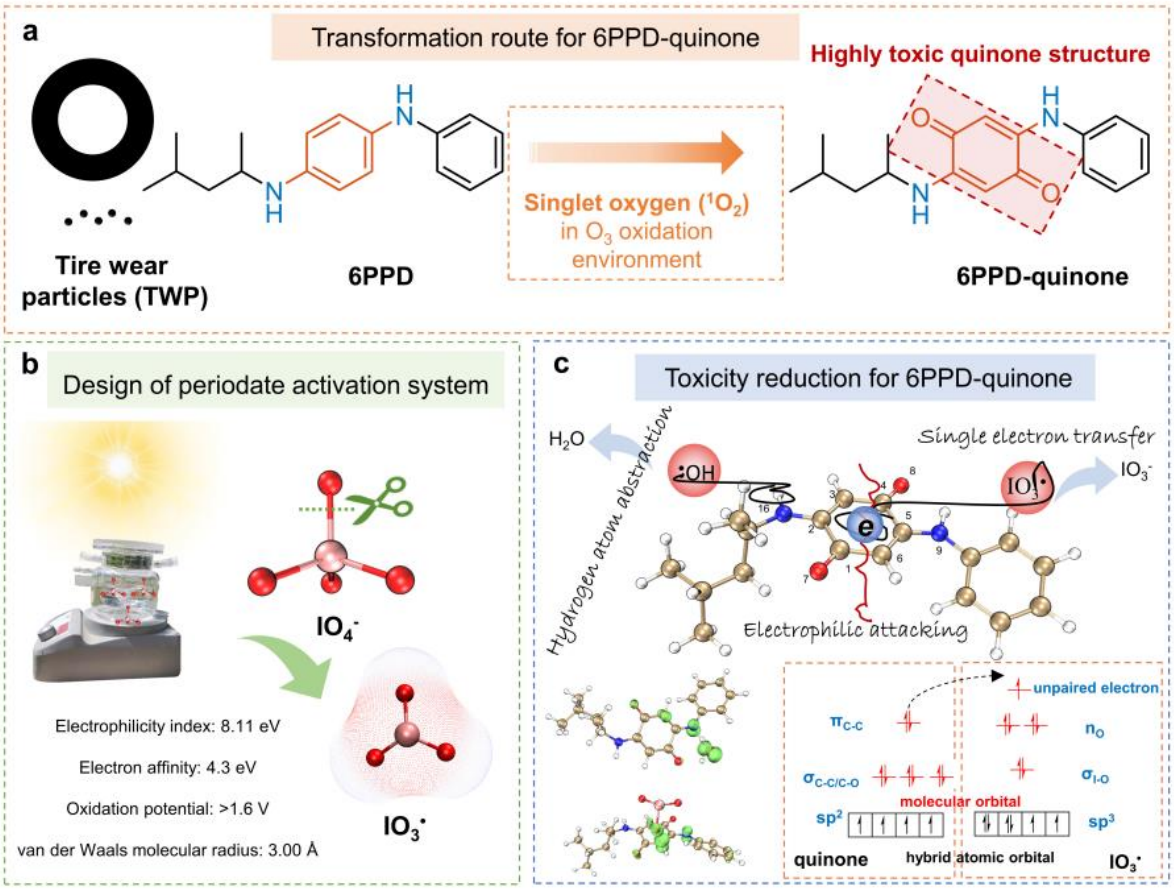

Fig. 1 Schematic diagram showing the construction of the periodate activation system for degradation of 6PPD-quinone. a, Transformation route from 6PPD to 6PPD-quinone through ozonation in the environment. **b,** Design of solar-light-driven periodate activation system and properties of generated $IO_3^{\bullet}$. **c,** Degradation of 6PPD-quinone under attack from $IO_3^{\bullet}$ and $^{\bullet}OH$.

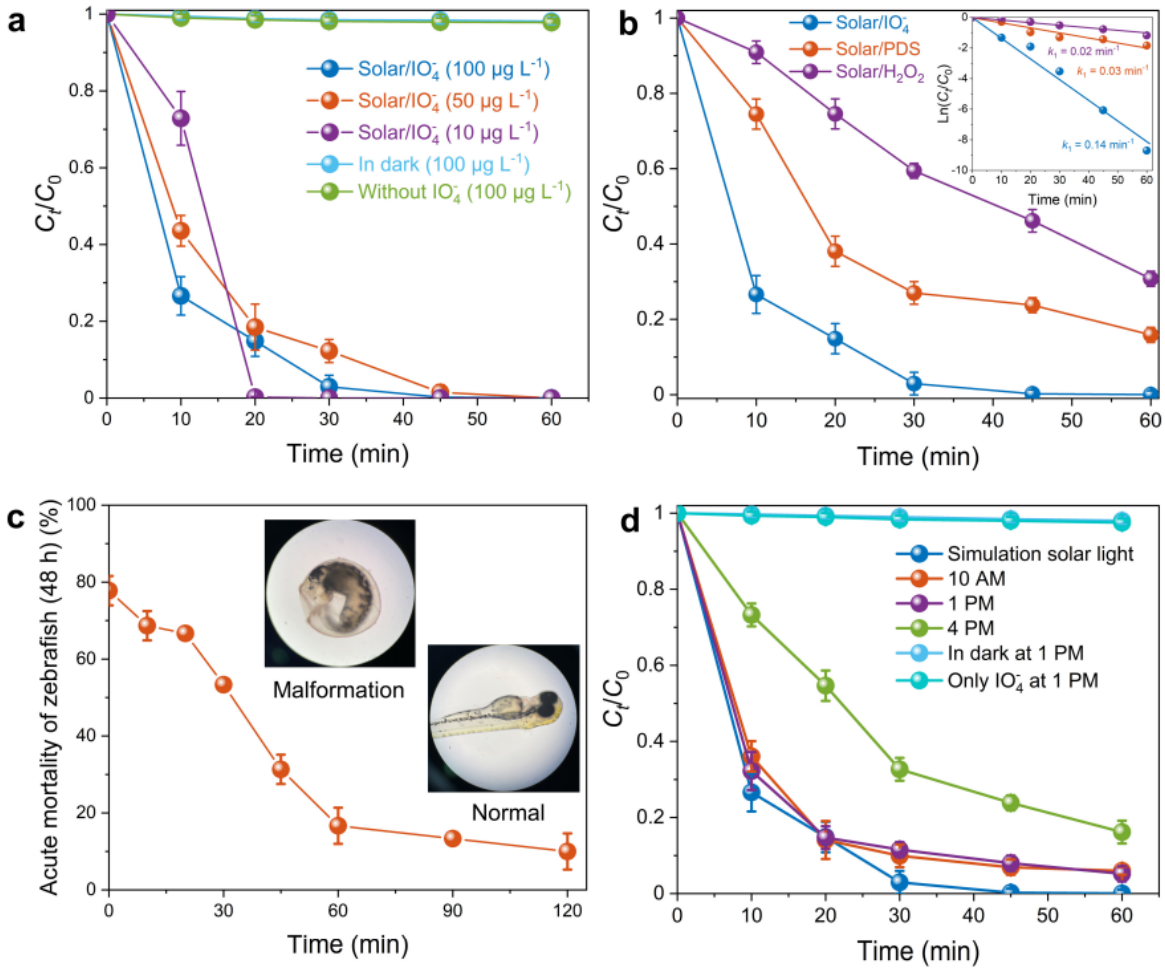

Fig. 2 Degradation and toxicity reduction of 6PPD-quinone by solar light activating periodate. a, Degradation kinetics of 6PPD-quinone in the solar/IO_4^- system. **b,** Degradation kinetics of 6PPD-quinone in solar/IO_4^-, solar/PDS and solar/H_2O_2 systems. **c,** Acute mortality of zebrafish (48 h) after addition of degradation water samples in the solar/IO_4^- system at predetermined time intervals. **d,** Degradation performance of 6PPD-quinone under natural solar light. Data are presented as mean values ± standard deviation from triplicate independent experiments (n = 3). Experimental conditions: pH = 5, [oxidant (IO_4^-, PDS or H_2O_2)] = 0.2 mmol L^{-1}; [6PPD-quinone] = 100, 50, or 10 μg L^{-1} for **a**, [6PPD] = 100 μg L^{-1} for **b-d**.

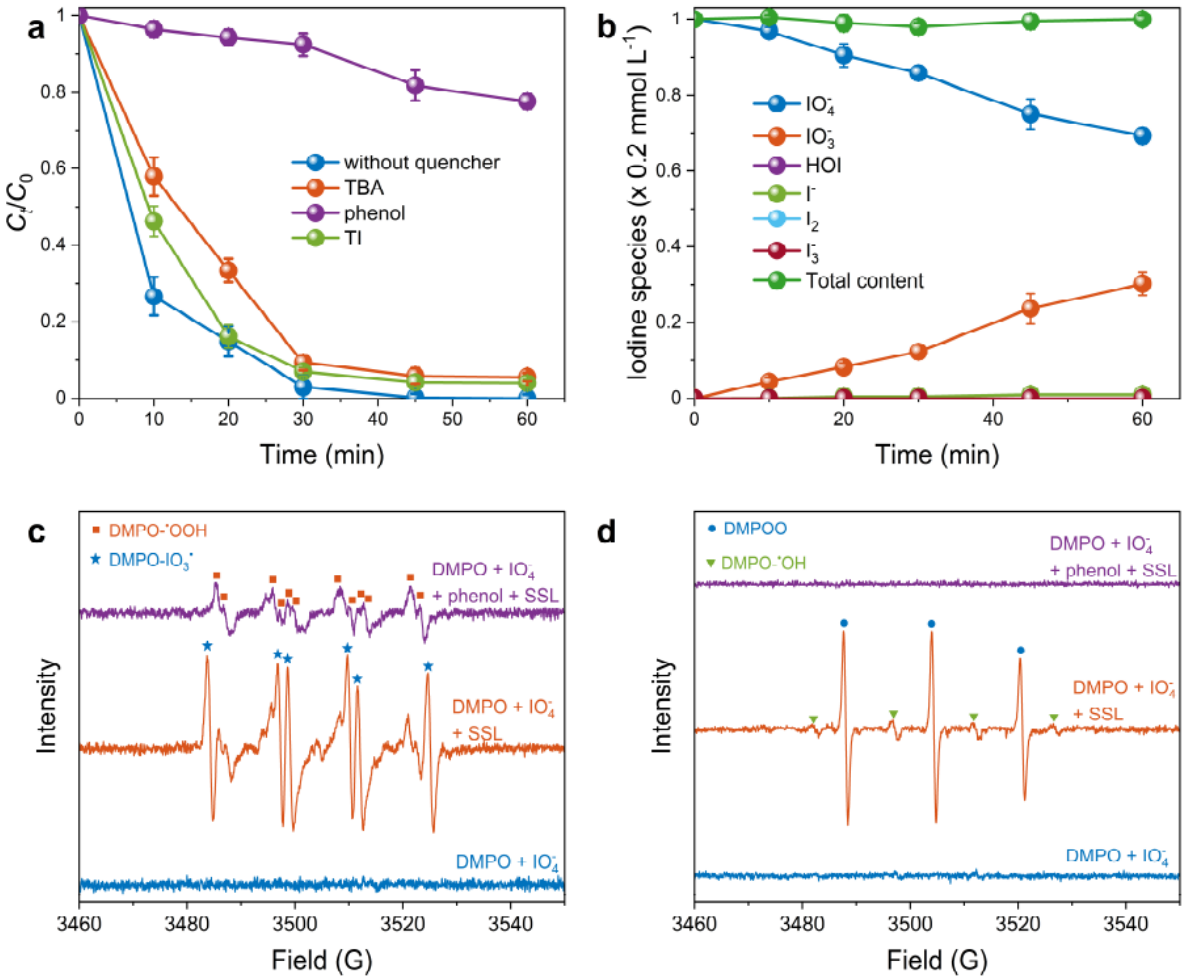

Fig. 3 The contribution and identification of reactive species on the degradation of 6PPD-quinone in the solar/IO_4^- system. a, Influence of different scavengers on 6PPD-quinone degradation. **b,** Conversion of iodine-related species during the reaction. **c,** EPR spectra of DMPO-$^{\bullet}$OOH and DMPO-$IO_3^{\bullet}$ in DMSO (SSL: simulated solar light). **d,** EPR spectra of DMPO-$^{\bullet}$OH and DMPOO in water. Data in **a** and **b** are presented as mean values ± standard deviation from triplicate independent experiments (n = 3). Experimental conditions: pH = 5, [IO_4^-] = 0.2 mmol L^{-1}, [6PPD-quinone] = 100 μg L^{-1}; [scavenger] = 50 mmol L^{-1} for **a**, [DMPO] = 100 mmol L^{-1} for **c** and **d**.

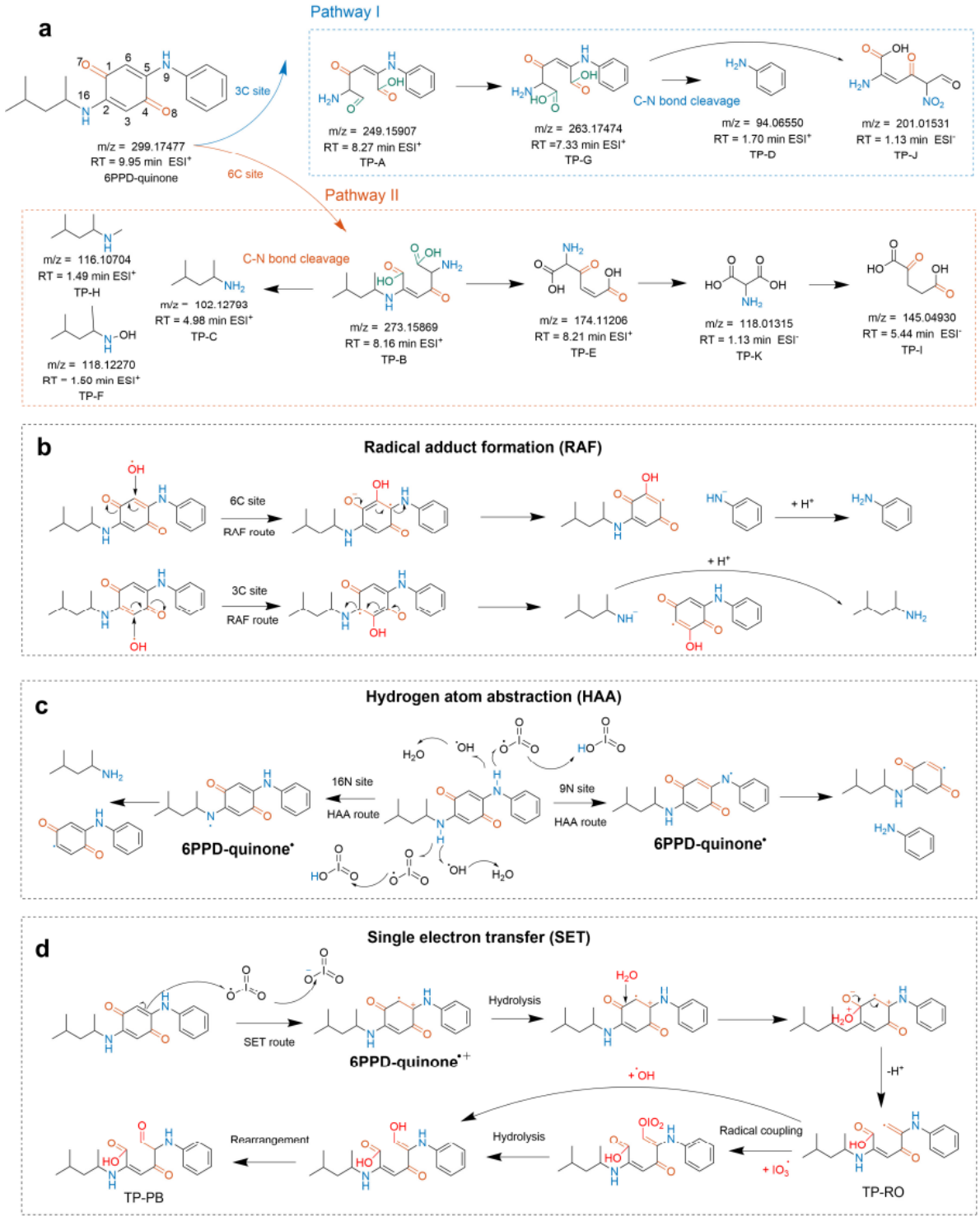

Fig. 4 Degradation pathway of 6PPD-quinone and typical initial reaction for destruction of quinone structure. a, Proposed degradation pathway of 6PPD-quinone in the solar/IO_4^- system. **b,** Radical adduct formation route for •OH. **c,** Hydrogen atom abstraction route for IO_3• and •OH. **d,** Single electron transfer reaction for IO_3•.

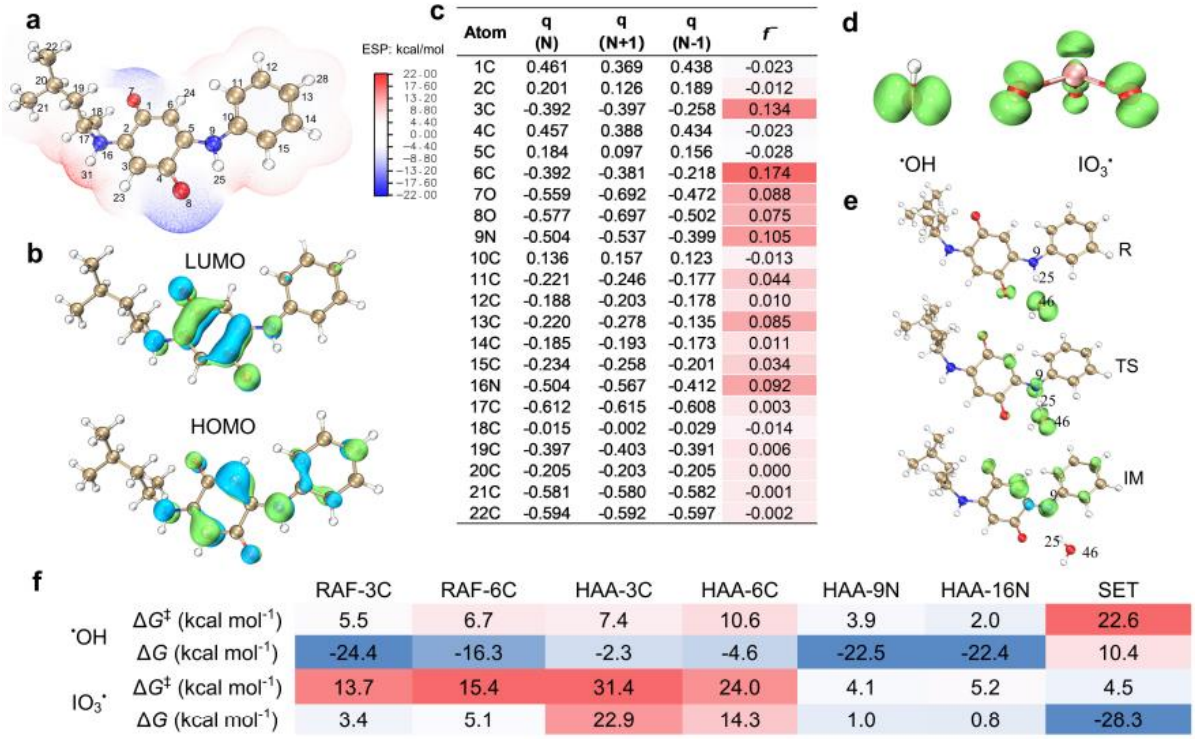

Atom	q (N)	q (N+1)	q (N-1)	f^-
1C	0.461	0.369	0.438	-0.023
2C	0.201	0.126	0.189	-0.012
3C	-0.392	-0.397	-0.258	0.134
4C	0.457	0.388	0.434	-0.023
5C	0.184	0.097	0.156	-0.028
6C	-0.392	-0.381	-0.218	0.174
7O	-0.559	-0.692	-0.472	0.088
8O	-0.577	-0.697	-0.502	0.075
9N	-0.504	-0.537	-0.399	0.105
10C	0.136	0.157	0.123	-0.013
11C	-0.221	-0.246	-0.177	0.044
12C	-0.188	-0.203	-0.178	0.010
13C	-0.220	-0.278	-0.135	0.085
14C	-0.185	-0.193	-0.173	0.011
15C	-0.234	-0.258	-0.201	0.034
16N	-0.504	-0.567	-0.412	0.092
17C	-0.612	-0.615	-0.608	0.003
18C	-0.015	-0.002	-0.029	-0.014
19C	-0.397	-0.403	-0.391	0.006
20C	-0.205	-0.203	-0.205	0.000
21C	-0.581	-0.580	-0.582	-0.001
22C	-0.594	-0.592	-0.597	-0.002

f

		RAF-3C	RAF-6C	HAA-3C	HAA-6C	HAA-9N	HAA-16N	SET
•OH	$\Delta G^{\ddagger}$ (kcal mol^{-1})	5.5	6.7	7.4	10.6	3.9	2.0	22.6
	ΔG (kcal mol^{-1})	-24.4	-16.3	-2.3	-4.6	-22.5	-22.4	10.4
IO_3•	$\Delta G^{\ddagger}$ (kcal mol^{-1})	13.7	15.4	31.4	24.0	4.1	5.2	4.5
	ΔG (kcal mol^{-1})	3.4	5.1	22.9	14.3	1.0	0.8	-28.3

Fig. 5 Reactive sites of electrophilic attack and energy change for HAA and SET routes. **a**, ESP distribution of 6PPD-quinone. **b**, HOMO and LUMO distributions of 6PPD-quinone. **c,** Natural population analysis (NPA) of charge distribution (q) and condensed Fukui index (f^-) representing electrophilic attack on 6PPD-quinone. **d,** Spin densities of •OH and IO_3•. **e,** Spin density distribution of reactants (R), transition states (TS), and intermediates (IM) during 6PPD-quinone degradation through HAA reaction at 9N site by •OH. **f,** Hot map of Gibbs free energy change (ΔG) and reaction activation energy ($\Delta G^{\ddagger}$) for typical reaction routes.

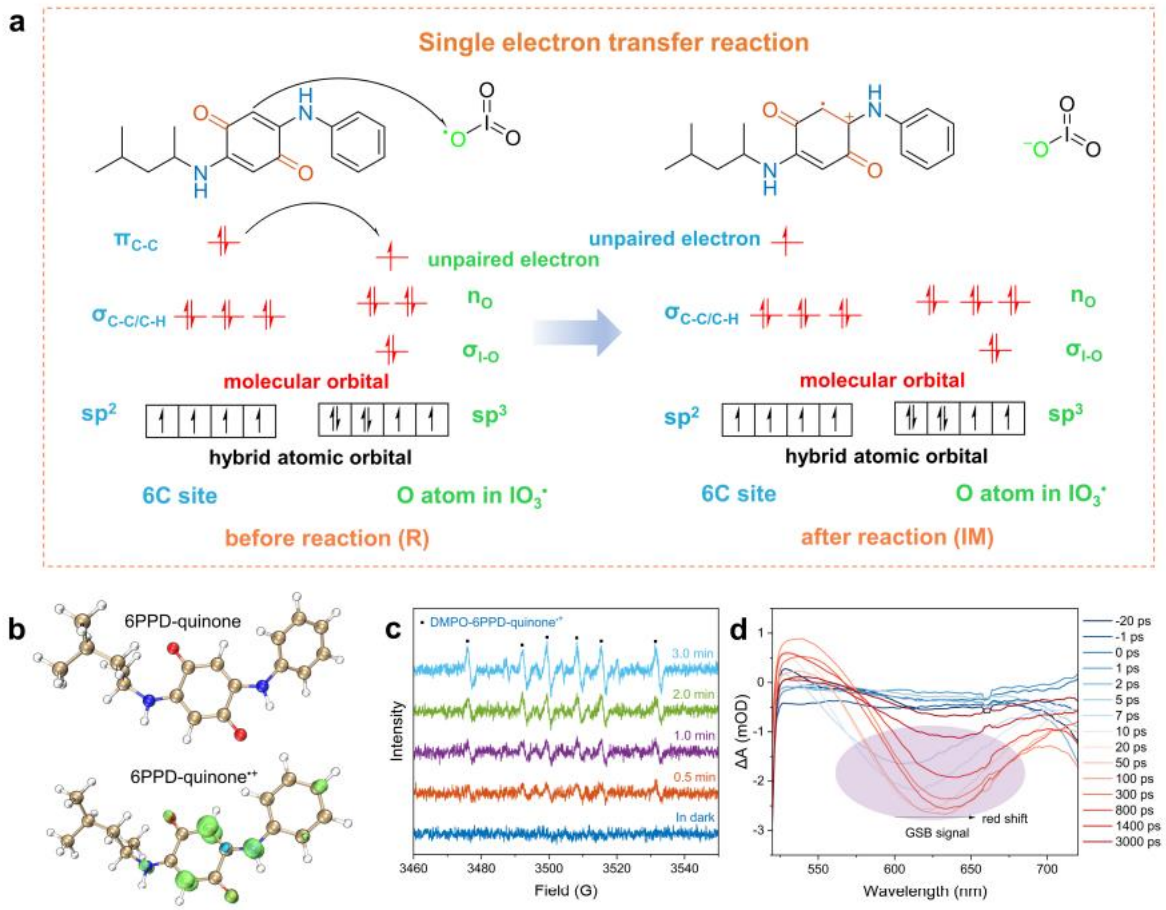

Fig. 6 Single electron transfer mechanism from 6PPD-quinone to $IO_3^{\bullet}$. a, SET reaction mechanism for 6PPD-quinone oxidation by $IO_3^{\bullet}$ at 6C site based on dynamic analysis of the electron distribution at the molecular orbital level. **b,** Calculated spin density of 6PPD-quinone and 6PPD-quinone$^{\bullet+}$. **c,** EPR spectra of detected 6PPD-quinone cationic radical. **d,** Femtosecond transient absorption spectra (fs-TAS) of 6PPD-quinone$^{\bullet+}$ in the time range of the IO_4^- activation system (λ_{exc} = 320 nm).